communications chemistry

ARTICLE

https://doi.org/10.1038/s42004-022-00779-0 OPEN

Effects of ligand tuning and core doping of atomically precise copper nanoclusters on CO_2 electroreduction selectivity

Mei Ding[1], Li Tang[1], Xiaoshuang Ma[1✉], Caixia Song[1✉] & Shuxin Wang[1✉]

Atomically precise nanoclusters (NCs) provide opportunities for correlating the structure and electrocatalytic properties at atomic level. Herein, we report the single-atom doping effect and ligand effect on CO_2 electroreduction (eCO_2RR) by comparing monogold-doped Au_1Cu_{24} and homocopper Cu_{25} NCs protected by triphenylphosphine or/and tris(4-fluorophenyl) phosphine. Catalytic results revealed that the electronic distribution of Cu_{25} NCs is enormously contracted by doping Au atoms, entitling it to exhibit the unique inhibition of hydrogen evolution reaction. And the inductive effect of ligand strongly favors the formation of formate in eCO_2RR. Overall, this work will provide guidance for the rational design of the copper-based catalysts in the eCO_2RR.

[1] College of Materials Science and Engineering, Qingdao University of Science and Technology, Qingdao 266042, P. R. China. ✉email: xiaoshuang_ma@qust.edu.cn; songcaixia@qust.edu.cn; shuxin_wang@qust.edu.cn

Electrochemical CO_2 reduction reaction (eCO_2RR) has been attracting intensive research efforts, as it can convert CO_2 to value-added chemicals in a carbon neutral route[1–4]. Due to the chemical inertness of CO_2, sufficient activation energy is necessarily needed for breaking C–O bond and producing new carbon chemicals. Therefore, it is imperative for us to develop efficient catalysts to lower activation energy. So far, several transition metal-based catalysts have been successfully synthesized with high activity, but the specific selectivity for reduction products is relatively poor[5,6].

Ligand-protected atomically precise metal nanoclusters (NCs) have been widely used in the field of catalysis[7–12], owing to their unique properties and well-defined structures[13]. Recently, the catalysis application has expanded to eCO_2RR to explore the formation mechanism of the reduction products, involving morphology[14], active center[15–20], size effect[21], alloy effect[22–25], electronic structure[26,27], ligand type[28–31], and so on. To be specific, Wang and co-workers reported that $[Au_{22}H_3(dppe)_3(PPh_3)_8]^{3+}$ exhibited higher selectivity towards CO ($FE = 92.7\%$ at -0.6 V) than that of $[Au_{11}(dppe)_5]^{3+}$ ($FE = 70.6\%$), in which the former was consisted of two Au_{11} units, indicating the structure of NCs plays an important role in electrochemical performance[32]. For another case, $Pt_1Au_{37}(SCH_2Ph^tBu)_{24}$ (15 electrons) was fabricated by doping mono-Pt into the kernels of $Au_{38}(SCH_2Ph^tBu)_{24}$ (14 electrons), leading to a broader HOMO-LUMO gap and increased selectivity of CO, while two Pt atoms doped $Pt_2Au_{37}(SCH_2Ph^tBu)_{24}$ (16 electrons) was less active than Pt_1Au_{37} for eCO_2RR[26]. Furthermore, fine tuning of the NCs surface by ligand modification could enhance the selectivity for eCO_2RR. For instance, Jin's group found that the thiolated Au_{25} NCs showed an excellent selectivity of CO_2 to CO, while the selenolated Au_{25} with the same metal packing inclined to the HER process[31]. Recently, Zang et al. reported that, $Au_{28}(C_2B_{10}H_{11}S)_{12}(C_4H_8S)_4Cl_4$ exhibited higher *FE* of CO (98.5%) than that of the alkynyl protected Au_{28} due to the stripping of surface ligand to expose more active sites[28].

Cu-based catalysts are considered to be the most promising eCO_2RR catalysts because of their suitable adsorption energy for CO_2 with H[33,34]. However, to our best knowledge, only a few cases about Cu NCs being used in eCO_2RR have been reported. For example, Jiang and co-works used $Cu_{32}H_{20}\{S_2P(O^iPr)_2\}_{12}$ as catalyst showing high selectivity of CO_2 to HCOOH ($FE = \sim90\%$), further verified that the HCOOH formation proceeds via the lattice-hydride mechanism through density functional theory calculations and experiments[35]. Subsequently, Zang's group found that the ditetrahedron-shaped Cu_8 NCs exhibited ultrahigh selectivity of HCOOH ($FE = \sim92\%$), which was twice as high as that of the cube-shaped Cu_8 NCs isomers[36]. Recently, our group reported that, the formation of surface hydride played a significant role in triggering the formation and stabilization of HCOO* on the Ag-Cu active center, leading to the exclusive formation of formate in the Cu-containing NCs[37]. However, hydrogen evolution reaction (HER), as the competing reaction of eCO_2RR, is inevitable in electroreduction with Cu-based NCs. Therefore, will the electronic distribution of NCs impact the composition of reduction products? How to effectively inhibit HER meanwhile promote eCO_2RR? What is the relationship between the selectivity of C_1 products (CO vs. HCOOH) and NCs structure? These questions form the aim and motivation of the current investigation.

Herein, we investigated the effects of the metal kernel and ligand on eCO_2RR at the atomic level by employing four different $[M@Cu_{24}H_{22}(PR_3)_{12}]^+$ (M = Au or Cu; R = -PPh_3 or -*p*-$FPPh_3$) NCs covered by two kinds of phosphine ligands, including $[Cu_{25}H_{22}(Ph_3P)_{12}]^+$ (Cu_{25}-$(Ph)_3P$ hereafter), $[Cu_{25}H_{22}(p\text{-}FPh_3P)_{12}]^+$ (Cu_{25}-$(p\text{-}FPh)_3P$ hereafter), $[AuCu_{24}H_{22}(Ph_3P)_{12}]^+$ ($AuCu_{24}$-$(Ph)_3P$ hereafter) and $[AuCu_{24}H_{22}(p\text{-}FPh_3P)_{12}]^+$ ($AuCu_{24}$-$(p\text{-}FPh)_3P$ hereafter). The Au-doped $M@Cu_{24}$ NCs show preference towards the products of the eCO_2RR, whereas homogeneous parent copper NCs tend to HER, indicating the metal dopants play a significant role in the electrochemical reactions. The kind of ligands also influences the selectivity of product in eCO_2RR. As a comparison, the NCs catalysts protected by fluoro-substituted phosphonate ligands gave rise to a more enhanced activity for the electrochemical process of CO_2-to-formate conversion at more positive potential. This work will provide guidance for the rational design of the copper-based catalysts for the eCO_2RR.

Results and discussion

Synthesis and characterization of $[M@Cu_{24}H_{22}(PR_3)_{12}]^+$ (M = Au or Cu; R = -PPh_3 or -*p*-$FPPh_3$) NCs. The four titled $M@Cu_{24}$ NCs were synthesized through our previously reported methods with minor modifications[38]. The $[Cu_{25}H_{22}(PPh_3)_{12}]Cl$ was firstly emerged as the by-product of Cu_{18} in C_6H_6 solvent reported by Hayton group[39]. In this work, compared with our previously reported method, we have improved the selectivity of these four target $M@Cu_{24}$ NCs through the synthetic modification, which was a high-temperature reduction method using sodium borohydride under inert atmosphere. Note that the minor modifications, which were critical for the formation of these four $M@Cu_{24}$ NCs with high yield. And we recorded the time-resolved UV–vis absorbance spectra of the four NCs to monitor the formation process, respectively. Note that, the absorption feature of Cu_{25}-$(Ph)_3P$ and $AuCu_{24}$-$(Ph)_3P$ are appeared at 1 h from the beginning (Supplementary Fig. 1a and 1b). Moreover, the four NCs could be controlled synthetized apace at 40 °C with high yields. For instance, the fingerprint absorbance peaks of tris(4-fluorophenyl) phosphine-protected $AuCu_{24}$-$(p\text{-}FPh)_3P$ (423 nm and 535 nm) and Cu_{25}-$(p\text{-}FPh)_3P$ (454 and 619 nm) are observed within 1 h of the reaction (Supplementary Fig. 1c and 1d). Polyhydrido copper clusters with Cu(0) character obtained by high-temperature reduction, which may be due to the Cu–H bond heterolysis and Cu atoms nucleation promoted by the fast Pedesis.

In our previous work, the crystal structure and optical properties of the four NCs have been compared[38]. According to these reported crystallographic information and X-ray crystallography analysis of four clusters[38,39], the four NCs have quite similar $M@Cu_{12}@Cu_{12}$ metal framework and surface motif arrangements (Fig. 1), providing an ideal platform to probe the electronic structure effect of the catalysts on the eCO_2RR. All the four NCs share the same 13-atom $M@Cu_{12}$ (M = Cu or Au) icosahedron kernel, which is covered by four $Cu_3(R_3P)_3$ units (i.e., $Cu_3(Ph_3P)_3$ or $Cu_3(p\text{-}FPh_3P)_3$). The detailed synthetic procedure can be found in the "Methods" section, and the relevant characterization elucidation will be discussed next.

The electron distribution and composition of the four NCs can be revealed by UV–vis spectra and X-ray photoelectron spectroscopy (XPS). As displayed in Supplementary Fig. 2a and 2c, Cu_{25}-$(Ph)_3P$ shows two distinct absorption peaks located at around 459 and 635 nm, while Cu_{25}-$(p\text{-}FPh)_3P$ presents a little bit blue-shift (454 and 619 nm), due to electron-withdrawing ligands leading to an increased band gap. Similar absorption peak blue-shift also occurs in $AuCu_{24}$-$(Ph)_3P$ (437 and 580 nm) and $AuCu_{25}$-$(p\text{-}FPh)_3P$ (423 and 535 nm) (Supplementary Fig. 2b and 2d). Moreover, the two mono-Au-doping alloy NCs are brown in dichloromethane, in contrast with both Cu_{25}-$(Ph)_3P$ and Cu_{25}-$(p\text{-}FPh)_3P$ presenting a light green visible to the naked eye. The electronic structures of these four NCs were subsequently probed by X-ray photoelectron spectroscopy (XPS), and the results are

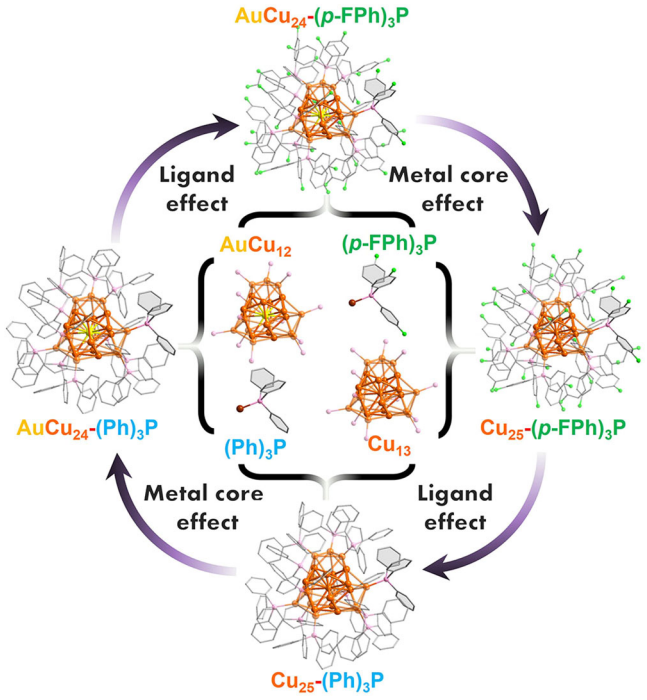

Fig. 1 Total structures and anatomy of Cu_{25}-$(Ph)_3P$, Cu_{25}-$(p$-$FPh)_3P$, $AuCu_{24}$-$(Ph)_3P$ and $AuCu_{24}$-$(p$-$FPh)_3P$. Color code: orange, Cu; yellow, Au; green, F; violet, P; gray, C. The H atoms are omitted for clarity.

presented in Supplementary Figs. 3, 4 and Supplementary Table 1. As depicted in Supplementary Figs. 3a, 3c, 4a and 4c, the XPS survey scan profiles confirmed the co-existence of the Cu, P, and C elements in Cu_{25}-$(Ph)_3P$; the Au, Cu, P, and C elements in $AuCu_{24}$-$(Ph)_3P$; Cu, P, F and C elements in Cu_{25}-$(p$-$FPh)_3P$; Au, Cu, P, F and C elements in $AuCu_{24}$-$(p$-$FPh)_3P$, respectively. The Au/Cu atomic ratio of $AuCu_{24}$-$(Ph)_3P$ and $AuCu_{24}$-$(p$-$FPh)_3P$ were estimated as 1.03/24.15 and 1.16/24.21, in good agreement with the theoretical value (1/24). As illustrated in Supplementary Figs. 3b, 3d, 4b and 4d, the binding energies of Cu $2p_{3/2}$ peaks in $AuCu_{24}$-$(Ph)_3P$ (932.56 eV) and $AuCu_{24}$-$(p$-$FPh)_3P$ (932.62 eV) are much higher than that of Cu_{25}-$(Ph)_3P$ (932.42 eV) and Cu_{25}-$(p$-$FPh)_3P$ (932.48 eV), suggesting that one gold atom doped can significantly affect the electron distribution of the parent homogenous Cu_{25} NCs. Compared with homogenous Cu_{25} NCs, the free valence electrons of the $AuCu_{12}$ core enormously shrunk inward by one gold doping, leading to a fact that Cu on the surface were electropositive. Furthermore, the binding energy of relatively electron-withdrawing ligands covered $AuCu_{24}$-$(p$-$FPh)_3P$ (932.62 eV) was slightly higher than that of $AuCu_{24}$-$(Ph)_3P$ (932.56 eV), and it means that more electropositive Cu atoms could be observed in relatively electron-withdrawing ligands coved M@Cu_{24} NCs. Meanwhile, the binding energies of the Au $4f_{7/2}$ peaks in $AuCu_{24}$-$(p$-$FPh)_3P$ (84.14 eV) and $AuCu_{24}$-$(p$-$FPh)_3P$ (84.48 eV) are on a higher-energy side (oxidation side) relative to that of Au(0) (84.0 eV), demonstrating that the incorporated Au is partially oxidized (Supplementary Figs. 3e and 4e).

Electrocatalytic CO_2 reduction performance. Electrochemical CO_2 reduction reaction (shorted for eCO_2RR) was envisioned to measure the catalytic performances of these title NCs. Given the abundant surface defects and functional groups of acid multi-walled carbon nanotubes (CNTs), the four NCs were deposited onto CNTs with 50% wt. loading to form the $AuCu_{24}$-$(Ph)_3P$/CNTs, Cu_{25}-$(Ph)_3P$/CNTs, $AuCu_{24}$-$(p$-$FPh)_3P$/CNTs and Cu_{25}-$(p$-$FPh)_3P$/CNTs electrocatalysts. Noted that, no nanoparticles were observed on the surface of four electrocatalysts, which corresponds to the X-ray diffraction (XRD) pattern (Supplementary Fig. 5). It was found that CO and H_2 were the only two gaseous products under all applied potential (without IR correction) versus the reversible hydrogen electrode (RHE) by gas chromatography (GC). In addition, ^{1}H-NMR spectra verified liquid products (Supplementary Fig. 6). The linear scanning voltammetry (LSV) were first conducted for the four catalysts. As depicted in Supplementary Fig. 7, both $AuCu_{24}$-$(Ph)_3P$/CNTs and $AuCu_{24}$-$(p$-$FPh)_3P$/CNTs exhibit a much higher current density and a more positive onset potential in CO_2 saturated aqueous 0.5 M $KHCO_3$ solution than in the one of N_2 purged, indicating that the two mono-Au-doped clusters have much higher CO_2 reduction activity. Cu_{25}-$(Ph)_3P$/CNTs and Cu_{25}-$(p$-$FPh)_3P$/CNTs, almost the same current density are observed at all of the test potentials, implying that HER rather than eCO_2RR is the major reduction process for both Cu_{25} NCs electrocatalysts.

For these four electrocatalysts, one-metal-atom and ligand difference can cause remarkable eCO_2RR catalytic performance discrepancy, and a strong metal core effect (Cu_{13} vs. $AuCu_{12}$) and ligand effect (Ph_3P vs. FPh_3P) is observed. As illustrated in Fig. 2a–c, $AuCu_{24}$-$(Ph)_3P$/CNTs exhibits the highest CO faradaic efficiency (FE_{CO}) of 45.6% at −1.0 V, while H_2 is the main product (FE_{H2} >80%) of the Cu_{25}-$(Ph)_3P$/CNTs in all tested potential ranges and the FE of CO and formate is only ~0–3.7% and ~6.1–10.1% at −0.8 to −1.0 V. It was due to the core effect (Au vs. Cu), suggesting that the mono-gold doped $AuCu_{24}$ can selectively reduce CO_2 to high value-added carbon products. In contrast, the homogeneous Cu-based NCs, because of the high Cu-H binding energy, could be the active center for HER. Similarly, $AuCu_{24}$-$(p$-$FPh)_3P$/CNTs and Cu_{25}-$(p$-$FPh)_3P$/CNTs, which had only one-metal-atom difference from each other, displayed FE_{CO} content only 11.8% to 20.6% and 2.1% to 8.2% in the entire tested potential, respectively (Fig. 2d). However, compared with triphenylphosphine covered NCs, $AuCu_{24}$-$(p$-$FPh)_3P$/CNTs ($FE_{formate}$ = 30.6%) and Cu_{25}-$(p$-$FPh)_3P$/CNTs ($FE_{formate}$ = 20.3%) have higher FE of formate, which were several times more than that of $AuCu_{24}$-$(Ph)_3P$ and Cu_{25}-$(Ph)_3P$ (Fig. 2e). Futhermore, the selectivity btween C_1 and H_2 product of Cu_{25}-$(p$-$FPh)_3P$/CNTs (FE_{H2} = 80.2 to 90.4%) and $AuCu_{24}$-$(p$-$FPh)_3P$/CNTs (FE_{H2} = 59.3–70.6%) are similiar with triphenylphosphine counterparts (Fig. 2f). As shown in the Fig. 2g, the $FE_{CO+formate}$ on $AuCu_{24}$-$(Ph)_3P$/CNTs of 55.9% is almost four times more than that of Cu_{25}-$(Ph)_3P$/CNTs ($FE_{CO+formate}$ = 14.8%) at the tested potential of −0.8 V, while the Cu_{25}-$(p$-$FPh)_3P$/CNTs had lower $FE_{CO+formate}$ (20.8%), which were about a half that of $AuCu_{24}$-$(p$-$FPh)_3P$/CNTs ($FE_{CO+formate}$ = 40.5%) (Fig. 2h). Noted that, the formate selectivity on the two tris(4-fluorophenyl)phosphine protected NCs were two times more than that of $AuCu_{24}$-$(Ph)_3P$/CNTs and Cu_{25}-$(Ph)_3P$/CNTs, indicating that the ligand effect had a momentous effect on selectively reducing CO_2 to C_1 products.

Meanwhile, the CO partial current density (j_{CO}) increased with the increasement of applied potential for the four electrocatalysts (Supplementary Fig. 8a and 8d). Both of mono-gold-doped NCs had a much larger j_{CO} value than those of Cu_{25}-$(Ph)_3P$/CNTs and Cu_{25}-$(p$-$FPh)_3P$/CNTs at all potentials, further manifesting unique advantage of Au-doped NCs for converting CO_2 into CO exclusively. Furthermore, the partial current density of formate ($j_{formate}$) for $AuCu_{24}$-$(Ph)_3P$/CNTs and Cu_{25}-$(Ph)_3P$/CNTs increased with the increasement of tested potential (Supplementary Fig. 8b). However, the $j_{formate}$ of the two tris(4-fluorophenyl)phosphine covered NCs exhibited the same trend with each other, that is, it first increased then decreased, and the maximal value is 3.2 mA cm^{-2} for Cu_{25}-$(p$-$FPh)_3P$/CNTs and

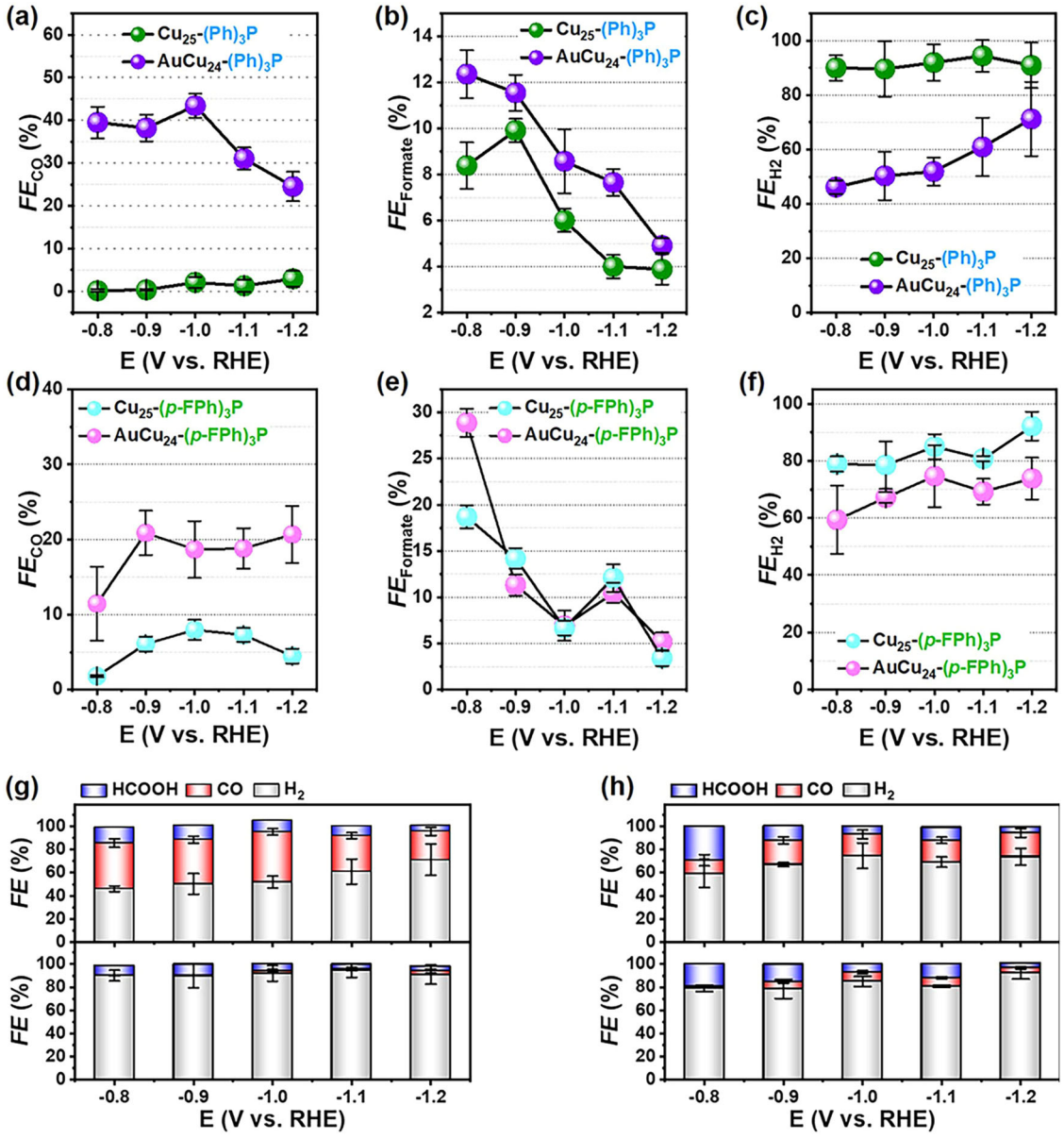

Fig. 2 The electrocatalytic performance of the four M@Cu_{24} (M = Au/Cu) NCs in eCO_2RR. a, **d** CO, **b**, **e** formate and **c**, **f** H_2 faradaic efficiency of $AuCu_{24}$-$(Ph)_3P$, Cu_{25}-$(Ph)_3P$, and Cu_{25}-$(p$-$FPh)_3P$, $AuCu_{24}$-$(p$-$FPh)_3P$, respectively. FEs for various eCO_2RR products obtained on **g** $AuCu_{24}$-$(Ph)_3P$, Cu_{25}-$(Ph)_3P$, and **h** $AuCu_{24}$-$(p$-$FPh)_3P$, Cu_{25}-$(p$-$FPh)_3P$. The error bars represent the standard deviation of three tests at the same test potential.

2.6 mA cm^{-2} for $AuCu_{24}$-$(p$-$FPh)_3P$/CNTs at −1.1 V, which is much higher than that of triphenylphosphine counterparts (Supplementary Fig. 8e). This is mainly attributed to that the HER process became dominant at more negative potentials. Note that, both of Au-doped NCs had smaller partial current density of H_2 (j_{H2}) than that of corresponding Cu_{25} NCs, indicating that one gold atom doping could increase the selectivity for deducing CO_2 to C_1 product (Supplementary Fig. 8c and 8f).

Stability is a significant index for evaluating well-defined NCs electrocatalysts in eCO_2RR, hence the long-term stability of the four catalysts were tested at −0.8 V, respectively. As illustrated in Fig. 3a, d, the current density and corresponding FE value of two mono-Au doped NCs remained almost unchanged (j_{total} = −7.13 to −6.91 mA cm^{-2} for $AuCu_{24}$-$(Ph)_3P$/CNTs; j_{total} from −7.05 to −6.90 mA cm^{-2} for $AuCu_{24}$-$(p$-$FPh)_3P$/CNTs) after 12 hours of continuous operation, indicating robust long-term durability. However, under the same conditions, the current density of Cu_{25}-$(Ph)_3P$/CNTs and Cu_{25}-$(p$-$FPh)_3P$/CNTs decreased about 5.7% (from −4.04 to −3.81 mA cm^{-2}) and 4.3% (from −4.90 to −4.69 mA cm^{-2}), respectively. Meanwhile, the $FE_{CO+formate}$ and FE_{H2} of the four electrocatalysts are almost unchanged during the whole time (Fig. 3b, c, e, f). Furthermore, the morphologies of these NCs after eCO_2RR are almost the same as before (Supplementary Fig. 9). These results indicate that, the majority of NCs electrocatalysts can be well preserved during the eCO_2RR process. Using the fingerprint absorbance peak (635 nm for Cu_{25}-$(Ph)_3P$/CNTs; 580 nm for $AuCu_{24}$-$(Ph)_3P$/CNTs; 619 nm for Cu_{25}-$(p$-$FPh)_3P$/CNTs; 535 nm for $AuCu_{24}$-$(p$-$FPh)_3P$/CNTs) as the metric, the absorbance change can be quantified and employed to estimate the recovery rate (Supplementary Fig. 10). Notably, the entire absorbance feature of the four NCs kept constantly, though the intensity of the characteristic peaks was decreased at varying degrees under different potentials. At the −0.8 V, all the recovery rate of four catalysts were over 50%, which was in good agreement with the finding in the *i*-t test and the calculated results as summarized in Supplementary Table 2.

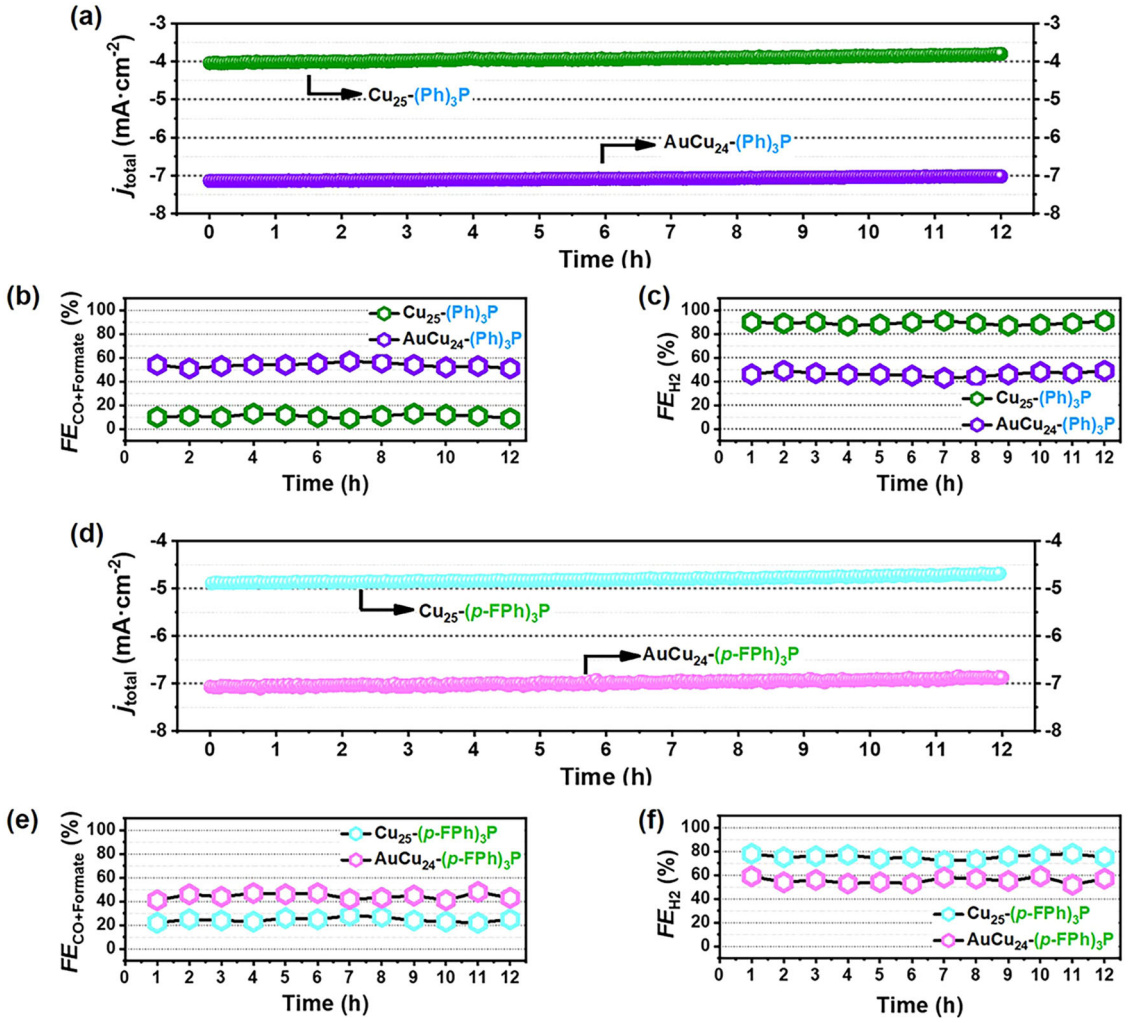

Fig. 3 Long-term stability of Cu_{25}-$(Ph)_3P$, $AuCu_{24}$-$(Ph)_3P$, Cu_{25}-$(p\text{-}FPh)_3P$ and $AuCu_{24}$-$(p\text{-}FPh)_3P$ at −0.80 V. a, **d** i-t curve; FEs of **b**, **e** C_1 products and **c**, **f** H_2 at different time.

The electrochemically active surface area (ECSA) was measured to further reveal the reason for the difference in the catalytic performance of the four clusters in eCO_2RR. The current density of Cu_{25}-$(Ph)_3P$, $AuCu_{24}$-$(Ph)_3P$, Cu_{25}-$(p\text{-}FPh)_3P$, and $AuCu_{24}$-$(p\text{-}FPh)_3P$ at different scan rate ranging from 20 to 100 mV s^{-1} were recorded and shown in Supplementary Fig. 11, and based on that, the double-layer capacitance (C_{dl}) of the four NCs were evaluated to be 1.27, 1.21, 0.99 and 0.94 mF, respectively. Thus, the ECSA of Cu_{25}-$(Ph)_3P$, $AuCu_{24}$-$(Ph)_3P$, Cu_{25}-$(p\text{-}FPh)_3P$, and $AuCu_{24}$-$(p\text{-}FPh)_3P$ were calculated to be 31.75, 30.25, 24.75 and 23.50 cm^2, respectively. Therefore, the number of active sites of the three clusters can be arranged in descending order as Cu_{25}-$(Ph)_3P$ > $AuCu_{24}$-$(Ph)_3P$ > Cu_{25}-$(p\text{-}FPh)_3P$ > $AuCu_{24}$-$(p\text{-}FPh)_3P$, which was attributed to the number of active sites scales with the ligand removal. Furthermore, the electrochemical impedance (EIS) was carried out to explore the charge transport properties of the four NCs at the electrode/electrolyte interface (Supplementary Fig. 12). The Nyquist plot of both homogeneous Cu_{25} NCs exhibited a much smaller the semicircular diameters than that of mono-gold-doped $AuCu_{24}$, and the former have a conductivity with lower interfacial charge-transfer resistance.

Effect on electron-density distribution modulating of copper catalyst on the selectivity of C_1 products (CO vs. formate) from eCO_2RR. According to the catalytic performance above, we find that the metal core plays an important role in the two competitive reactions (HER vs. eCO_2RR) in electroreduction selectivity, further, achieving the formation selectivity for C_1 products (formate vs. CO) in eCO_2RR by changing the ligand type. Get insight in the electron-density distribution of the M@Cu_{24} (Au/ Cu), as displayed in Fig. 4, core and ligand effect could be observed: (i) the Cu atom on the surface of mono-gold-doped $AuCu_{24}$ have lower electron cloud density (δ^+) and is more prone to eCO_2RR, caused by the free valence electrons of the $AuCu_{12}$ core to shrink inward; (ii) The more electro-positive Cu atoms banding with electrophilic ligand are pre-ferable to bind the O atom of CO_2, and showing selectivity for formate. Experimentally, the XPS results reflected the positive charge distribution among the four NCs. By mono-gold doping, the exterior Cu atoms of $AuCu_{24}$-$(Ph)_3P$ (932.56 eV) and $AuCu_{24}$-$(p\text{-}FPh)_3P$ (932.62 eV) are much more electropositive than that of Cu_{25}-$(Ph)_3P$ (932.42 eV) and Cu_{25}-$(p\text{-}FPh)_3P$ (932.48 eV) (Supplementary Figs. 3b, 3d, 4b and 4d). It was noting that, HER was inevitable for the polyhydrido Cu NCs catalysts in electrochemical reduction, however, it was advisable to increase the selectivity toward to eCO_2RR and reduce the H-source supply in the solution by electron-contracted element such as Au, Pt, Pd, etc. More importantly, using electrophilic ligand could not only raise the stability of NCs, and promote the selectivity of formate in eCO_2RR.

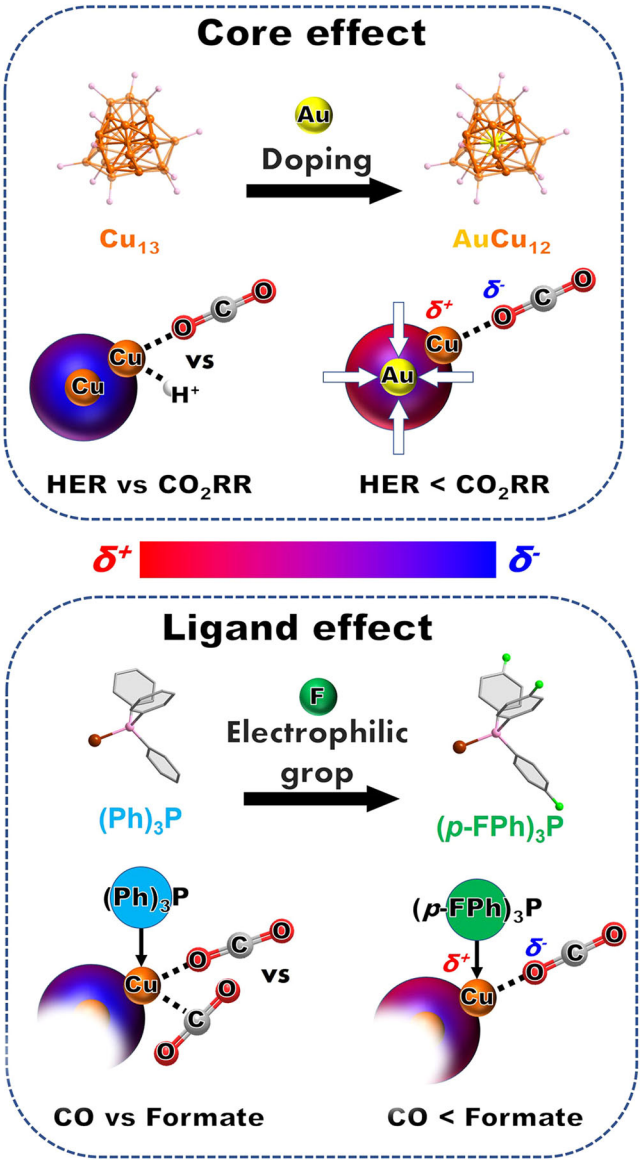

Fig. 4 The scheme of electron distribution modulating on NCs by ligand tuning and core doping. a Core effect (Cu_{13} vs. $AuCu_{12}$) and **b** ligand effect (triphenylphorsphine vs. tris(4-fluorophenyl)phosphine).

Conclusion

In summary, these four polyhydrido M@Cu_{24} (M = Au or Cu) NCs were controllably synthesized and used as electrocatalysts to probe the core and ligand effect for electroreduction selectivity. Significantly, the inert metal doping was propitious to eCO_2RR, and the modification of the electrophilic ligand was efficient to enhance the selectivity for formate in eCO_2RR. This work not only provides an efficient and simple strategy to prepare the polyhydrido Cu-based NCs, but also highlights the unique advantages of employing metal NCs as model catalysts to advance the fundamental mechanistic understanding toward electroreduction and beyond.

Methods

Chemicals and materials. The cupric (II) acetylacetonate ($C_{10}H_{14}O_4Cu$), tetrachloroauric (III) acid ($HAuCl_4{\cdot}3H_2O$, >99.99% metals basis), triphenylphosphine (Ph_3P, ≥99%), tris(4-fluorophenyl)phosphine ((*p*-FPh)$_3$P, ≥99%), $NaBH_4$ (>98%) were received from Aldrich (Shanghai, China). Methanol, dichloromethane, and n-hexane were purchased from Aldrich (Shanghai, China). All reagents and solvents were commercially available and used without further purification. Pure water was purchased from Wahaha Co. Ltd. All glassware was thoroughly cleaned with aqua regia (HCl:HNO_3 = 3:1, v-v), rinsed with copious pure water.

Synthesis of $[Cu_{25}H_{22}(Ph_3P)_{12}]^+$ nanoclusters (Cu_{25}-(Ph)$_3$P). Firstly, Cu_{25}-(Ph)$_3$P NCs were prepared according to a reported protocol with some minor modifications[38]. Briefly, at 40 °C under Ar atmosphere, a solution of cupric(II) acetylacetonate (60 mg) dissolved in a mixed solvent of methanol and dichloromethane in a volume ratio of 3:1. The color of the solution was ink blue. After 30 min, triphenylphosphine (100 mg) was added, and the solution changed slowly from ink blue to light blue. After that, 2 mL freshly aqueous $NaBH_4$ (0.66 M in ice-cold water) was quickly added under vigorous stirring. The color of the solution slowly changed from light blue to yellow-green within 10 min. The reaction was aged for 2.5 h at room temperature. The solvent was then evaporated to give a yellow-green solid. After the reaction, the volume of the mixture was evaporated to dryness to give a black solid, which was successively washed with n-hexane and diethyl ether to remove the byproducts and excess triphenylphosphine, followed by extraction with dichloromethane and then dried by rotary evaporation. After diffusion of n-hexane to a dichloromethane solution at −4 °C for about one week, black crystals were obtained (yield: ~40% based on copper salt).

Synthesis of the $[Cu_{25}H_{22}((p\text{-}FPh)_3P)_{12}]^+$ nanoclusters (Cu_{25}-(*p*-FPh)$_3$P). The synthesis of Cu_{25}-(*p*-FPh)$_3$P was similar to that of Cu_{25}-(Ph)$_3$P and the synthetic procedures are identical until the addition of ligand, which triphenylphosphine was replaced with tris(4-fluorophenyl)phosphine. After that, 2 mL freshly aqueous $NaBH_4$ (0.66 M in ice-cold water) was quickly added under vigorous stirring. The reaction was aged for 10 h at room temperature. After the reaction, the volume of the mixture was evaporated to dryness to give black solid, which was successively washed with n-hexane and diethyl ether to remove the byproducts and excess ligands, followed by extraction with dichloromethane and then dried by rotary evaporation. After diffusion of n-hexane to a dichloromethane solution at −4 °C for about two days, black crystals were obtained (yield: ~70% based on copper salt).

Synthesis of $[AuCu_{24}H_{22}(Ph_3P)_{12}]^+$ nanoclusters ($AuCu_{24}$-(Ph)$_3$P). Firstly, $AuCu_{24}$-(Ph)$_3$P was synthesized following the methods reported by us previously with some minor modifications[38]. Briefly, at 40 °C under Ar, a solution of cupric(II) acetylacetonate (60 mg) and $HAuCl_4{\cdot}3H_2O$ (5 mg) dissolved in mixed solvent of methanol and dichloromethane in a volume ratio of 3:1. The color of the solution was ink blue. After 30 min, triphenylphosphine (100 mg) was added and the solution changed slowly from ink blue to light blue. After that, 2 mL freshly aqueous $NaBH_4$ (0.66 M in ice-cold water) was quickly added under vigorous stirring. The color of the solution quickly turned reddish brown. The reaction was aged for 10 h at room temperature. The solvent was then evaporated to give a yellow-green solid. After the reaction, the volume of the mixture was evaporated to dryness to give black solid, which was successively washed with n-hexane and diethyl ether to remove the byproducts and excess triphenylphosphine, followed by extraction with dichloromethane and then dried by rotary evaporation. After diffusion of n-hexane to a dichloromethane solution at −4 °C for about three days, black crystals were obtained (yield: ~30% based on copper salt).

Synthesis of $[AuCu_{24}H_{22}(p\text{-}FPh_3P)_{12}]^+$ nanoclusters ($AuCu_{24}$-(*p*-FPh)$_3$P). The synthesis of $AuCu_{24}$-(*p*-FPh)$_3$P was similar to that of $AuCu_{24}$-(Ph)$_3$P and the synthetic procedures are identical until the addition of ligand, which triphenylphosphine was replaced with tris(4-fluorophenyl)phosphine. Then, 2 mL freshly aqueous $NaBH_4$ (0.66 M in ice-cold water) was quickly added under vigorous stirring. The color of the solution quickly turned reddish brown. The reaction was aged for 10 h at 40 °C. The solvent was then evaporated to give a reddish-brown solid. After the reaction, the volume of the mixture was evaporated to dryness to give a black solid, which was successively washed with n-hexane and diethyl ether to remove the byproducts and excess ligands, followed by extraction with dichloromethane and then dried by rotary evaporation. After diffusion of n-hexane to a dichloromethane solution at −4 °C for about three days, black crystals were obtained (yield: ~80% based on copper salt).

Electrochemical measurements. To prepare the catalyst sample, these four as-prepared M@Cu_{24} (M = Au/Cu) were loading on acidic multi-walled carbon (CNTs) with a mass ratio of 1 (5 mg NC and 5 mg CNTs). The catalyst ink was prepared by dispersing the sample in isopropyl alcohol under sonication for 5 min. Then 1 mL catalyst suspension and 10 μL Nafion (5 wt.%) were uniformly mixed as the final catalyst ink. Then, 40 μL catalytic ink was dropwise cast onto the carbon cloth (1.0 × 1.0 cm^2) and dried at room temperature as the working electrode. All electrochemical measurements were carried out in a custom gas-tight H-cell with two compartments separated by Nafion 117 membrane. Each compartment contained 25 mL electrolyte (0.5 M $KHCO_3$: pH = 7.2 when saturated with CO_2, pH = 8.8 when saturated with N_2) with ~10 mL headspace. The electrochemical measurements were carried out on an electrochemical workstation (CHI 760E) with Pt sheet as counter electrode and Ag/AgCl electrodes (KCl saturated) as

reference electrode. All the potentials were calibrated to a reversible hydrogen electrode (RHE) according to the Nernst equation:

$$R(\mathrm{RHE}) = \mathrm{E(Ag/AgCl)} + 0.059 \times \mathrm{pH} + 0.197 \quad (1)$$

The output of the gas flow from the cathode chamber was directed into a gas chromatograph instrument (GC3900Plus, RUI NENG) for identification and quantification of the gaseous products, which was purged for 30 min with an average rate of 10 mL min^{-1} (at room temperature and ambient pressure) prior to the test. The GC was installed with a thermal conductivity detector (TCD) to detect H_2 and flame ionization detector (FID) to detect hydrocarbons. A methanizer (Agilent) was equipped in front of the FID for CO detection. High-purity Argon (99.9999%) was used as the carrier gas for all compartments of the GC.

The faradaic efficiency (FE_X) and corresponding partial current density (j_X) of X (X = CO or H_2 or formate) were calculated as below:

$$\mathrm{FE}_X = \frac{(N_i \times \mathrm{n} \times \mathrm{F})}{Q_t} \quad (2)$$

$$j_X = \frac{\mathrm{FE}_X \times Q_t}{\mathrm{t} \times \mathrm{Area}} \quad (3)$$

Where

Q_t = total charge consumed in the electrochemical reaction

N_i = the number of moles of the product (measured GC) n = the number of electrons transferred in the elementary reaction (n is 2 for CO, H_2 and formate)

F = the Faradaic constant (96485 C mol^{-1})

t = reaction time (s)

Area = geometry area of the electrode (1 cm^2)

The electrochemically active surface area (ECSA) of the catalyst was obtained via the linear fit of the corresponding current density with respect to the scan rate (Fig. S10). The results show that double layer capacitance of electrode (C_{dl}) for Cu_{25}-$(Ph)_3P$, $AuCu_{24}$-$(Ph)_3P$, Cu_{25}-$(p\text{-}FPh)_3P$ and $AuCu_{24}$-$(p\text{-}FPh)_3P$ are 1.27, 1.21, 0.99 and 0.94 mF, respectively. The ESCA can be calculated based on the following formula:

$$\mathrm{ECSA} = \frac{C_{\mathrm{dl}}}{C_s} \quad (4)$$

where C_S is the specific capacitance of the sample or capacitance of an atomically smooth planar surface of the material per unit area under identical electrolyte conditions. And the average C_S value of 0.04 mF cm^{-2} for an ideal flat surface of the metal catalyst in alkaline solution reported by McCrory was chosen for the ECSA evaluation[40].

For the morphology of four catalysts before and after eCO_2RR, the NCs/CNTs loaded work electrodes were directly conducted by SEM measurement. For stability, the NCs/CNTs loaded carbon fibers were as work electrodes. The eCO_2RR was allowed to proceed at −0.8 V (vs. RHE) for 30 min. After the test, the samples were rinsed with dichloromethane and collected for UV–vis characterization.

General characterization. The surface chemical compositions and valence states were examined by X-ray photoelectron spectroscopy (XPS, Phi X-tool instrument). Scanning electronic microscopic (SEM) images were collected with a field-emission scanning electron microscope (FESEM, Merlin). UV–visible absorption spectra of clusters, dimer and tetramer were recorded on a Shimadzu 2600/2700 spectrophotometer.

Data availability

All data generated or analyzed during this study are included in this article (and its Supplementary Information files).

Received: 1 September 2022; Accepted: 15 November 2022;
Published online: 19 December 2022

References

1. Wagner, A., Sahm, C. D. & Reisner, E. Towards molecular understanding of local chemical environment effects in electro- and photocatalytic CO_2 reduction. *Nat. Catal.* **3**, 775–786 (2020).
2. Birdja, Y. Y. et al. Advances and challenges in understanding the electrocatalytic conversion of carbon dioxide to fuels. *Nat. Energy* **4**, 732–745 (2019).
3. Wu, J., Sharifi, T., Gao, Y., Zhang, T. & Ajayan, P. M. Emerging carbon-based heterogeneous catalysts for electrochemical reduction of carbon dioxide into value-added chemicals. *Adv. Mater.* **31**, e1804257 (2019).
4. Quan, Y., Zhu, J. & Zheng, G. Electrocatalytic reactions for converting CO_2 to value-added products. *Small Sci.* **1**, 2100043 (2021).
5. Nitopi, S. et al. Progress and perspectives of electrochemical CO_2 reduction on copper in aqueous electrolyte. *Chem. Rev.* **119**, 7610–7672 (2019).
6. Zou, Y. & Wang, S. An investigation of active sites for electrochemical CO_2 reduction reactions: from in situ characterization to rational design. *Adv. Sci.* **8**, 2003579 (2021).
7. Du, Y., Sheng, H., Astruc, D. & Zhu, M. Atomically precise noble metal nanoclusters as efficient catalysts: a bridge between structure and roperties. *Chem. Rev.* **120**, 526–622 (2020).
8. Yan, J., Teo, B. K. & Zheng, N. Surface chemistry of atomically precise coinage-metal nanoclusters: from structural control to surface reactivity and catalysis. *Acc. Chem. Res.* **51**, 3084–3093 (2018).
9. Yang, M. et al. Highly dispersed Bi clusters for efficient rechargeable Zn-CO_2 batteries. *Appl. Catal. B: Environ.* **307**, 121145 (2022).
10. Li, S. et al. The precise editing of surface sites on a molecular-like gold catalyst for modulating regioselectivity. *Chem. Sci.* **11**, 8000–8004 (2020).
11. Jin, R., Zeng, C., Zhou, M. & Chen, Y. Atomically precise colloidal metal nanoclusters and nanoparticles: fundamentals and opportunities. *Chem. Rev.* **116**, 10346–10413 (2016).
12. Jin, M. et al. Highly dispersed Ag clusters for active and stable hydrogen peroxide production. *Nano Res.* **15**, 5842–5847 (2022).
13. Yao, Q. F. et al. Molecular reactivity of thiolate-protected noble metal nanoclusters: synthesis, self-assembly, and applications. *Chem. Sci.* **12**, 99–127 (2021).
14. Zhao, S. et al. Influence of atomic-level morphology on catalysis: the case of sphere and rod-like gold nanoclusters for CO_2 electroreduction. *ACS Catal.* **8**, 4996–5001 (2018).
15. Qin, L. et al. Homoleptic alkynyl-protected Ag_{15} nanocluster with atomic precision: structural analysis and electrocatalytic performance toward CO_2 reduction. *Angew. Chem. Int. Ed.* **60**, 26136–26141 (2021).
16. Li, S. et al. Boosting CO_2 electrochemical reduction with atomically precise surface modification on gold nanoclusters. *Angew. Chem. Int. Ed.* **60**, 6351–6356 (2021).
17. Austin, N., Zhao, S., McKone, J. R., Jin, R. & Mpourmpakis, G. Elucidating the active sites for CO_2 electroreduction on ligand-protected Au_{25} nanoclusters. *Catal. Sci. Technol.* **8**, 3795–3805 (2018).
18. Alfonso, D. R., Kauffman, D. & Matranga, C. Active sites of ligand-protected Au_{25} nanoparticle catalysts for CO_2 electroreduction to CO. *J. Chem. Phys.* **144**, 184705 (2016).
19. Wan, X. K., Wang, J. Q. & Wang, Q. M. Ligand-protected Au_{55} with a novel structure and remarkable CO_2 electroreduction performance. *Angew. Chem. Int. Ed.* **60**, 20748–20753 (2021).
20. Sun, Y. N., Liu, X., Xiao, K., Zhu, Y. & Chen, M. Y. Active-site tailoring of gold cluster catalysts for electrochemical CO_2 reduction. *ACS Catal.* **11**, 11551–11560 (2021).
21. Seong, H. et al. Atomically precise gold nanoclusters as model catalysts for identifying active sites for electroreduction of CO_2. *Angew. Chem. Int. Ed.* **60**, 14563–14570 (2021).
22. Tang, S., Xu, J., Liu, X. & Zhu, Y. Ag doped Au44 nanoclusters for electrocatalytic conversion of CO_2 to CO. *Chem. -Eur. J.* **28**, e202201262 (2022).
23. Zhuang, S. et al. Hard-sphere random close-packed $Au_{47}Cd_2(TBBT)_{31}$ nanoclusters with a Faradaic efficiency of up to 96 % for electrocatalytic CO_2 reduction to CO. *Angew. Chem. Int. Ed.* **59**, 3073–3077 (2020).
24. Lin, X. et al. $[AuAg_{26}(SR)_{18}S]^-$ nanocluster: open shell structure and high Faradaic efficiency in electrochemical reduction of CO_2 to CO. *J. Phys. Chem. Lett.* **12**, 552–557 (2020).
25. Li, S. et al. Monopalladium substitution in gold nanoclusters enhances CO_2 electroreduction activity and selectivity. *ACS Catal.* **10**, 12011–12016 (2020).
26. Liu, X. et al. Asymmetrically doping a platium atom into a Au_{38} nanocluster for changing the electron configuration and reactivity in electrocatalysis. *Angew. Chem. Int. Ed.* **61**, e202207685 (2022).
27. Xu, J. Y. et al. Evolution from superatomic $Au_{24}Ag_{20}$ monomers into molecular-like $Au_{43}Ag_{38}$ dimeric nanoclusters. *Chem. Sci.* **13**, 2778–2782 (2022).
28. Wang, J., Xu, F., Wang, Z. Y., Zang, S. Q. & Mak, T. C. W. Ligand-shell engineering of a Au_{28} nanocluster boosts electrocatalytic CO_2 reduction. *Angew. Chem. Int. Ed.* **61**, e202207492 (2022).
29. Yuan, S. F. et al. Robust gold nanocluster protected with amidinates for electrocatalytic CO_2 reduction. *Angew. Chem. Int. Ed.* **60**, 14345–14349 (2021).
30. Kulkarni, V. K. et al. N-heterocyclic carbene-stabilized hydrido Au_{24} nanoclusters: synthesis, structure, and electrocatalytic reduction of CO_2. *J. Am. Chem. Soc.* **144**, 9000–9006 (2022).
31. Li, S. et al. The role of ligands in atomically precise nanocluster-catalyzed CO_2 electrochemical reduction. *Nanoscale* **13**, 2333–2337 (2021).
32. Gao, Z. H. et al. A heteroleptic gold hydride nanocluster for efficient and selective electrocatalytic reduction of CO_2 to CO. *J. Am. Chem. Soc.* **144**, 5258–5262 (2022).

33. Zhang, J.-N. et al. Copper as a single metal atom based photo-, electro- and photoelectrochemical catalyst decorated on carbon nitride surface for efficient CO_2 reduction: a review. *Nano Res. Energy* **1**, e9120015 (2022).
34. Ahmad, T. et al. Electrochemical CO_2 reduction to C_{2+} products using Cu-based electrocatalysts: a review. *Nano Res. Energy* **1**, e9120021 (2022).
35. Tang, Q. et al. Lattice-hydride mechanism in electrocatalytic CO_2 reduction by structurally precise copper-hydride nanoclusters. *J. Am. Chem. Soc.* **139**, 9728–9736 (2017).
36. Liu, L. J. et al. Mediating CO_2 electroreduction activity and selectivity over atomically precise copper clusters. *Angew. Chem. Int. Ed.* **61**, e202205626 (2022).
37. Ma, X. et al. Electrochemical CO_2 reduction catalyzed by atomically precise alkynyl-protected Au_7Ag_8, Ag_9Cu_6, and $Au_2Ag_8Cu_5$ nanoclusters: probing the effect of multi-metal core on selectivity. *Chem. Sci.* **13**, 10149–10158 (2022).
38. Chen, A. et al. Gram-scale preparation of stable hydride $M@Cu_{24}$ (M = Au/Cu) nanoclusters. *J. Phys. Chem. Lett.* **10**, 6124–6128 (2019).
39. Nguyen, T. A. et al. A Cu_{25} nanocluster with partial Cu(0) character. *J. Am. Chem. Soc.* **137**, 13319–13324 (2015).
40. McCrory, C. C., Jung, S., Peters, J. C. & Jaramillo, T. F. Benchmarking heterogeneous electrocatalysts for the oxygen evolution reaction. *J. Am. Chem. Soc.* **135**, 16977–16987 (2013).

Acknowledgements

We thank the financial support provided by the National Natural Science Foundation of China (22171156, 52072194 and 21803001), Taishan Scholar Foundation of Shandong Province (China), and Startup Funds from Qingdao University of Science and Technology.

Author contributions

S.W., C.S. and X.M. guided the whole experiment and conceived the idea. X.M. drafted the manuscript, M.D. conducted most of the experiments, L.T. gave some advice for the characterization and analysis, and C.S. and S.W. provided the funding support, and all the authors contributed to the final polishing of the manuscript.

Competing interests

The authors declare no competing interests.

Additional information

Supplementary information The online version contains supplementary material available at https://doi.org/10.1038/s42004-022-00779-0.

Correspondence and requests for materials should be addressed to Xiaoshuang Ma, Caixia Song or Shuxin Wang.

Peer review information *Communications Chemistry* thanks Zhenghua Tang and the other, anonymous, reviewer(s) for their contribution to the peer review of this work. Peer reviewer reports are available.